


Simultaneous Imaging of Magnetic Nanoparticle Concentration, Temperature, and Viscosity

Jing Zhong^{1,2,*}, Meinhard Schilling,¹ and Frank Ludwig¹

¹*Institut für Elektrische Messtechnik und Grundlagen der Elektrotechnik, TU Braunschweig, Braunschweig, Germany*

²*School of Instrumentation and Optoelectronic Engineering, Beihang University, Beijing, China*

 (Received 8 January 2021; revised 29 July 2021; accepted 14 October 2021; published 2 November 2021)

In the coming era of precision medicine, there is a high demand for the development of approaches for *in vivo* tracking of biomolecules and measurements of their local environments. In this work, we present an approach for the simultaneous imaging of magnetic nanoparticle (MNP) concentration, temperature, and viscosity. The proposed approach allows one to determine the spatial distribution of the MNPs, while the MNPs are used as nanosensors for simultaneous measurements of the spatial distributions of temperature and viscosity. This technique has great potential for providing not only tools for disease diagnostics and therapy, but also insights into further understanding of the biophysical mechanisms involved in tumor tissues during cancer development and tumor metastasis.

DOI: [10.1103/PhysRevApplied.16.054005](https://doi.org/10.1103/PhysRevApplied.16.054005)

I. INTRODUCTION

The development of alternative approaches for disease diagnostics and therapy plays a crucial role in promoting human healthcare from traditional medicine toward precision medicine. Stem-cell-based therapy has shown great promise in bone-marrow reconstitution for malignancies and aplasias [1–3]. In traditional drug delivery, such as chemotherapy, about 99% of the drugs do not reach the tumor tissue [4], which results in strong side effects. In contrast, targeted drug delivery aims at delivering the drugs to the intended tissue, thus improving the treatment efficiency and decreasing the side effects [5]. All these emerging techniques significantly contribute to precision medicine.

However, one of the most challenging issues for the implementation of these therapy methodologies is the *in vivo* efficient tracking and delivery of stem cells and drugs to the targeted tissue. Herein, a method for continuously monitoring the spatial distribution of the substances with noninvasiveness and high temporal resolution is of great importance to realize targeted delivery. One of the common methodologies for targeted delivery is the labeling and encapsulation of magnetic nanoparticles (MNPs) for delivery of or into cells [6,7] and the delivery of drugs [8], so that these substances can be *in vivo* tracked and controlled in magnetic fields. Thus, an approach based on MNP-concentration imaging with high sensitivity and high

temporal resolution is of great benefit to monitor the spatial distribution of the substances and to build a closed-loop system for active and efficient targeted delivery.

To implement precision medicine, another key point is the development of sensors for the determination of the microenvironmental parameters in specific tissues for disease diagnostics and therapy. For instance, temperature is one of the most fundamental physical parameters that reflects biological and physiological processes. Some specific diseases, such as malignant tumors, may result in a high-temperature region in the diseased tissue [9,10]. In magnetic hyperthermia, MNPs are exposed to a radio-frequency ac magnetic field to locally heat the tumor tissue for cancer therapy [11–13]. Herein, temperature is one of the most crucial parameters, significantly affecting treatment efficiency [14]. In addition, viscosity is one of the key parameters for maintaining vascular homeostasis [15–17]. An increase in blood viscosity may increase the risk of cardiovascular mortality [18,19]. The abnormal viscosity of blood can be a hallmark of specific diseases, e.g., Alzheimer's disease and inflammation [18,20]. Therefore, *in vivo* determination of temperature and viscosity is of great importance and interest not only to improve the efficiency of magnetic hyperthermia for cancer therapy but also of disease diagnostics and to understand the biophysical mechanisms taking place during disease.

An approach for the imaging of MNP concentration and the local environmental parameters of temperature and viscosity will significantly contribute to precision medicine with respect to disease diagnostics and therapy. The approach has to enable fast imaging for the

*j.zhong@tu-braunschweig.de

feasibility of building a closed-loop control system, to allow high sensitivity for accurate determination of the MNP concentration and to be versatile for simultaneous imaging of concentration, as well as the local microenvironmental temperature and viscosity. Furthermore, the approach should be noninvasive, nonradiative, and feasible to realize *in vivo* imaging.

Magnetic particle imaging (MPI) is an imaging modality that directly measures the spatial distribution of MNPs [21]. To date, several approaches have been reported to realize the imaging of MNP concentration [22–28]. MPI is proven to enable a high temporal resolution of up to about 50 three-dimensional (3D) images per second, high sensitivity in the order of 1 ng iron, and high spatial resolution better than 1 mm [29–32]. Furthermore, several publications have investigated the viscosity dependence of MNP dynamics by ac susceptibility and magnetic particle spectroscopy [zero-dimensional (0D) MPI] [33–39], showing the potential of MNPs to function as sensors for viscosity measurements. In 2018, multicolor MPI was used to realize viscosity quantification with a relative error of less than 6% [40,41]. However, the approach allowed one to quantify only the viscosity of a single MNP sample placed in the center of the imaging field of view, but not the spatial distribution of MNP samples with different viscosities at random positions. In 2019, another approach of relaxation-based color MPI was reported to realize the imaging of different relaxation times of five MNP samples with different viscosities [42], which could be converted into qualitative viscosity imaging. Thus, only quasi-quantitative viscosity imaging has been realized with color MPI. In addition to viscosity imaging, the magnetization curve [43–45], harmonics [46–48], and phase lag [49] were measured with 0D MPI systems to realize MNP thermometry, providing a sensor for robust, accurate, and noninvasive temperature measurements. Interestingly, the phase lag and harmonics are combined to realize MNP thermometry independent of Brownian relaxation [50]. In 2016, color MPI was used to realize qualitative two-dimensional (2D) temperature imaging [51], whereas, in 2018, scanning magnetic particle spectroscopy was investigated for quantitative 2D temperature imaging in addition to MNP-concentration imaging [27,52].

All the approaches for MPI employ MNP magnetization to realize concentration, temperature, and viscosity imaging. Specifically, for viscosity imaging, the frequency of the ac magnetic field should be high enough to show the dynamics dependence of MNP magnetization. This means that all three parameters of concentration, temperature, and viscosity of a MNP suspension significantly affect MNP magnetization. Herein, concentration is a parameter proportional to the signal strength or image intensity, whereas temperature and viscosity are nonlinear parameters that affect MNP magnetization and relaxation. Importantly, temperature and viscosity are two coupled physical

parameters, e.g., viscosity is dependent on temperature [53]. In color MPI, the measured images of relaxation time can be converted into only viscosity or temperature images but not to both. Ignoring any unexpected temperature variation during viscosity imaging may cause significant deviations in viscosity and vice versa. Thus, the simultaneous determination of temperature and viscosity significantly contributes to their accurate quantification. To date, there have been no approaches for the simultaneous and quantitative imaging of MNP concentration, temperature, and viscosity.

Here, we propose an approach for the simultaneous imaging of MNP concentration, temperature, and viscosity. It has great promise to provide a tool not only for cell tracking and drug delivery via MNP-concentration imaging, but also for magnetic hyperthermia-based cancer therapy and cardiovascular disease and inflammation diagnostics via temperature and viscosity imaging. The proposed approach employs the dynamic magnetization of MNPs dominated by Brownian relaxation to determine viscosity, since the Brownian (Néel) relaxation time is dependent on (independent of) environmental viscosity. Thus, for *in vivo* applications, the MNPs should be able to physically rotate in an ac magnetic field. Any contribution to the MNP's dynamic magnetization from Néel relaxation may lead to systematic errors in measured temperature and viscosity. Considering magnetic hyperthermia-based cancer therapy, the temperature range from 310 to 322 K is used for experiments. Since a higher viscosity may cause a Néel-relaxation contribution to the MNP's dynamic magnetization, to demonstrate the feasibility of the proposed approach for simultaneous imaging of MNP concentration, temperature, and viscosity, a smaller viscosity range from 0.95 to 1.46 mPa s at 22 °C (from 0.69 to 0.95 mPa s at 37 °C) is used for experiments. Dynamic magnetization of the MNPs dominated by Brownian relaxation is comprehensively analyzed based on solving the Fokker-Planck equation (FPE). It indicates that the first, third, and fifth harmonics of the MNPs, defining the i th harmonic as M_i at frequency ω_i , are determined by three independent parameters of MNP concentration, c ; the relaxation parameter, $\omega\tau_B$; and the Langevin parameter, ξ_0 (see detailed definitions in Sec. II). Herein, M_i , which is proportional to the concentration, c , can be used to visualize the spatial distribution of MNP concentration. The harmonic ratios $R_{3rd/1st} = M_3/M_1$ and $R_{5th/3rd} = M_5/M_3$, independent of the concentration, c , are nonlinear monotonous functions of $\omega\tau_B$ and ξ_0 . This means that the solutions of the nonlinear functions with measured $R_{3rd/1st}$ and $R_{5th/3rd}$ enable one to independently calculate $\omega\tau_B$ and ξ_0 . Consequently, temperature is determined from $\xi_0 = \mu_0 m H_{ac} / (k_B T)$, with the known temperature-dependent magnetic moment, m , and magnetic field amplitude, H_{ac} , whereas the viscosity at this temperature is determined from $\omega\tau_B$ with the calculated temperature. Therefore, here, we investigate the

nonlinear effects of $\omega\tau_B$ and ξ_0 on $R_{3rd/1st}$ and $R_{5th/3rd}$ by a phenomenological model and experiments. Finally, simultaneous imaging of the MNP concentration, temperature, and viscosity is realized by measuring the spatial distributions of the first, third, and fifth harmonics of the MNPs and applying the proposed phenomenological model.

II. MODEL AND METHOD

For MNPs dominated by Brownian relaxation, MNP magnetization in an ac magnetic field can be described by the FPE [54,55]:

$$\frac{\partial}{\partial t} W(x, t) = \frac{1}{2\tau_B} \frac{\partial}{\partial t} \times \left\{ (1 - x^2) \left[\frac{\partial}{\partial t} W(x, t) - \xi(t) W(x, t) \right] \right\}, \quad (1)$$

where $\xi(t) = \xi_0 \cos(\omega t)$, with $\xi_0 = \mu_0 m H_{ac} / (k_B T)$; $\tau_B = 3\eta V_h / (k_B T)$, with viscosity η and hydrodynamic volume of the MNPs V_h ; μ_0 is the magnetic permeability of free space; m is the MNP magnetic moment; k_B is the Boltzmann constant; T is the absolute temperature; $x = \cos\theta$, with θ representing the angle between the magnetic moment, m , and the applied magnetic field, H ; and $W(x, t)$ is the probability density of the magnetic moment orientations. Thus, MNP magnetization, $M(t)$, in the direction of the applied magnetic field, H , can be described by

$$M(t) = c M_s \int_{-1}^1 x W(x, t) dx, \quad (2)$$

where c is the MNP concentration. The FPE indicates that the i th harmonic amplitude, M_i , of MNP magnetization at frequency f_0 depends on three independent parameters: c , $\omega\tau_B$, and ξ_0 . The concentration, c , is a linear parameter, whereas $\omega\tau_B$ and ξ_0 are nonlinear parameters.

The FPE for Brownian relaxation indicates that dynamic magnetization of the MNPs dominated by Brownian relaxation depends only on the MNP concentration, c ; the Langevin parameter, ξ_0 ; and the relaxation parameter, $\omega\tau_B$. This means that the harmonic ratios of the third to the first harmonics and the fifth to the third harmonics are independent of MNP concentration, but depend only on ξ_0 and $\omega\tau_B$. However, the FPE does not have an analytical solution. Thus, the dependences of the MNP harmonics on parameters ξ_0 and $\omega\tau_B$ are not intuitive and not easily modeled. Furthermore, parameters ξ_0 and $\omega\tau_B$ are coupled to affect the MNP's dynamic magnetization and harmonics. Here, we propose a phenomenological model to describe

the harmonics ratios $R_{3rd/1st}$ and $R_{5th/3rd}$ as

$$R_{3rd/1st}(\omega\tau_B, \xi_0) = \frac{M_3}{M_1} = \frac{R_{3rd/1st}(0, \xi_0)}{1 + \alpha_{3rd/1st}(\omega\tau_B) + \beta_{3rd/1st}(\omega\tau_B)^2}, \quad (3a)$$

$$R_{5th/3rd}(\omega\tau_B, \xi_0) = \frac{M_5}{M_3} = \frac{R_{5th/3rd}(0, \xi_0)}{1 + \alpha_{5th/3rd}(\omega\tau_B) + \beta_{5th/3rd}(\omega\tau_B)^2}, \quad (3b)$$

where $\alpha_{3rd/1st}$, $\beta_{3rd/1st}$, $\alpha_{5th/3rd}$, and $\beta_{5th/3rd}$ are free parameters depending only on ξ_0 ; $R_{3rd/1st}(0, \xi_0)$ and $R_{5th/3rd}(0, \xi_0)$ represent the harmonic ratios at equilibrium. The proposed phenomenological model indicates that the effects of $\omega\tau_B$ and ξ_0 on $R_{3rd/1st}$ and $R_{5th/3rd}$ are decoupled by the free parameters $\alpha_{3rd/1st}$, $\beta_{3rd/1st}$, $\alpha_{5th/3rd}$, and $\beta_{5th/3rd}$ and the relaxation parameter $\omega\tau_B$. Using the parameters $\alpha_{3rd/1st}$, $\beta_{3rd/1st}$, $\alpha_{5th/3rd}$, $\beta_{5th/3rd}$, $R_{3rd/1st}(0, \xi_0)$, and $R_{5th/3rd}(0, \xi_0)$ and solving nonlinear Eqs. (3a) and (3b) with the measured $R_{3rd/1st}$ and $R_{5th/3rd}$ values allows one to independently calculate $\omega\tau_B$ and ξ_0 , thus resulting in the simultaneous determination of temperature and viscosity. Notably, the phenomenological model is only applicable for the dynamic magnetization of Brownian-relaxation-dominated MNPs. With a contribution to MNP magnetization from Néel relaxation, the phenomenological model may not be applicable due to systematic errors.

III. EXPERIMENTAL RESULTS

A. Experimental description

Here, SHP-25 MNPs, purchased from Ocean NanoTech. Ltd Corp. (San Diego, CA) and dominated by Brownian relaxation, are selected as the experimental sample. The sample consists of single-core iron-oxide nanoparticles with a mean core size of about 25 nm and an iron concentration of 5 mg/ml. Three samples with different viscosities, consisting of SHP-25 and glycerol with different weight percentages, c_{glycerol} , of 0.0%, 8.0%, and 13.3% are prepared. All samples have the same iron concentration of 3.33 mg/ml. The ac susceptibility (ACS) spectra of the three MNP samples are measured over the frequency range from 10 Hz to 1 MHz [56]. They show that, with increasing c_{glycerol} , the peak frequency, f_{peak} , of the imaginary parts, χ'' , of the ACS spectra, as expected, decreases due to the corresponding increase in the Brownian-relaxation time, τ_B . Given the viscosity of water, η_{water} , at 22 °C, the viscosities of the three MNP samples are 0.95, 1.26, and 1.46 mPa s at 22 °C, which fit very well with the theoretical viscosities of 0.96, 1.17, and 1.35 mPa s for the given c_{glycerol} [57]. The deviations in the measured and theoretical viscosities might be caused by the uncertainty

in the glycerin weight percentages. A custom-built scanning magnetic particle spectrometer (SMPS) is used to measure the first, third, and fifth harmonics in ac magnetic fields with different frequencies and amplitudes. The SMPS consists of a pair of Helmholtz coils for the generation of ac magnetic fields and a gradiometric detection coil with a diameter of about 2.5 mm for the measurement of MNP magnetization. A digital lock-in algorithm is used to measure the harmonics of MNP magnetization. Details of the SMPS can be found in Ref. [27].

B. Magnetic-field-dependent harmonic ratio

To verify the feasibility of the phenomenological model, $R_{3rd/1st}$ and $R_{5th/3rd}$ of the three MNP samples with different viscosities are measured in ac magnetic fields with

different frequencies, f_0 , and amplitudes, H_{ac} , at a constant temperature of 310.45 K (37.3 °C). Frequency f_0 is varied from 615 to 1418 Hz, whereas amplitude H_{ac} is changed from 5 to 8 mT. Figures 1(a) and 1(b) show $R_{3rd/1st}$ and $R_{5th/3rd}$ versus frequency curves of the three MNP samples versus frequency f_0 at $H_{ac}=8$ mT. With increasing frequency and viscosity, the harmonic ratios $R_{3rd/1st}$ and $R_{5th/3rd}$ decrease, as expected from simulations of the FPE. $R_{3rd/1st}$ and $R_{5th/3rd}$ versus f curves at different H_{ac} are fitted by Eq. (3). Good fits of the phenomenological model to experimental data, as shown in Figs. 1(a) and 1(b), demonstrate the feasibility of the phenomenological model for the description of the harmonic ratios. Furthermore, the fits also allow one to determine the viscosity of the samples relative to the viscosity of water at 37.3 °C. For the given viscosity of water at 37.3 °C, the viscosities of the

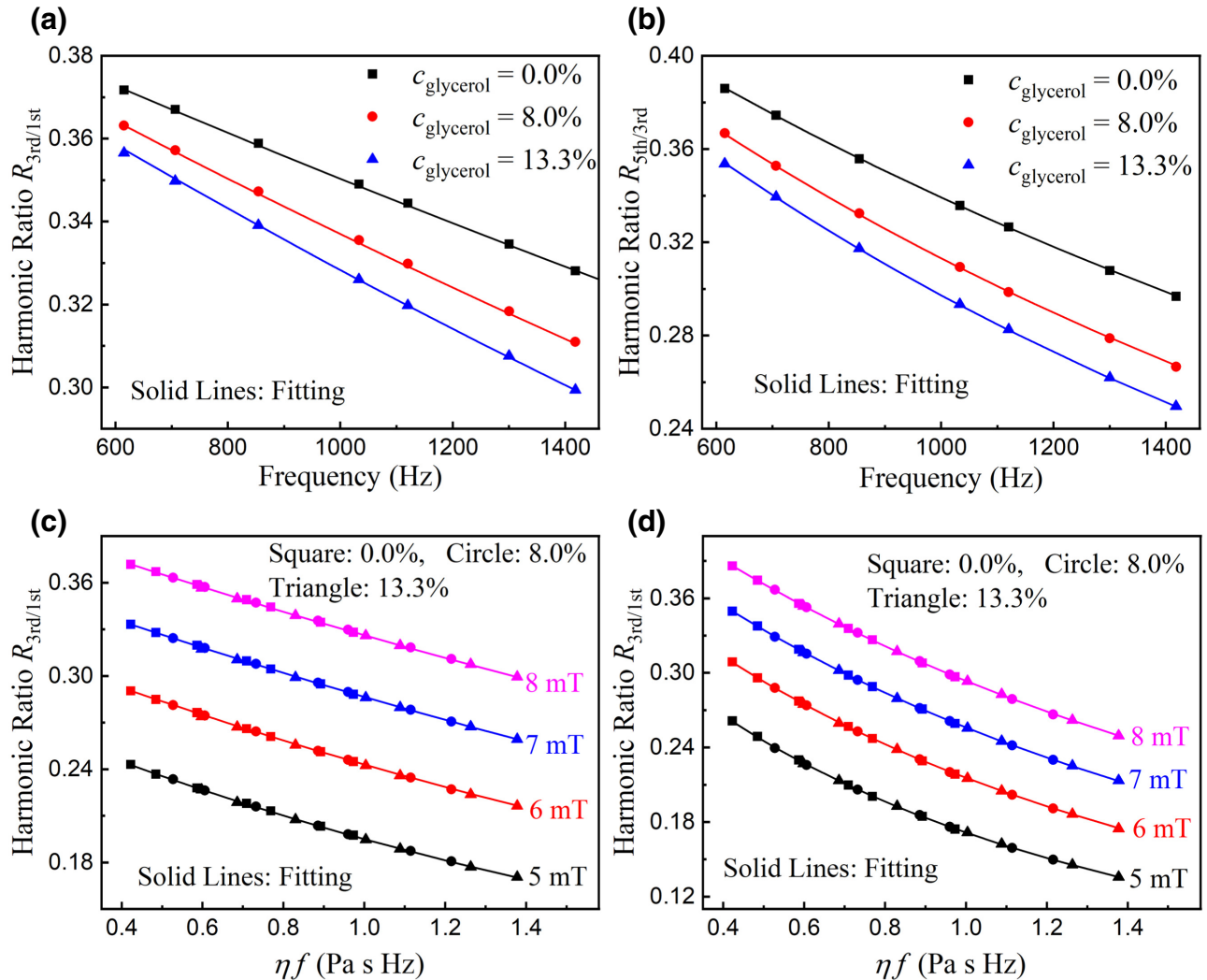


FIG. 1. Experimental results of harmonic ratios $R_{3rd/1st}$ (a) and $R_{5th/3rd}$ (b) versus frequency for samples with different weight percentages of glycerin in different frequencies of ac magnetic fields with an amplitude of 8 mT at 37.3 °C. Experimental results of harmonic ratios $R_{3rd/1st}$ (c) and $R_{5th/3rd}$ (d) versus ηf in different frequencies of ac magnetic fields with varying amplitudes at 37.3 °C. Symbols are experimental results, whereas solid lines are fits with Eq. (3).

three samples are 0.69, 0.86, and 0.97 mPa s, respectively, which fit very well to the theoretical values (0.69, 0.83, and 0.95 mPa s).

In addition, Figs. 1(c) and 1(d) show $R_{3rd/1st}$ and $R_{5th/3rd}$ versus ηf at different H_{ac} , showing that the curves of the three MNP samples collapse into a single curve at the same H_{ac} . This demonstrates the independence of the free parameters $\alpha_{3rd/1st}$, $\beta_{3rd/1st}$, $\alpha_{5th/3rd}$, and $\beta_{5th/3rd}$ of the relaxation parameter, $\omega\tau_B$, and the feasibility of the proposed phenomenological model for decoupling the effects of $\omega\tau_B$ and ξ_0 on $R_{3rd/1st}$ and $R_{5th/3rd}$. Herein, the parameters $\alpha_{3rd/1st}$, $\beta_{3rd/1st}$, $\alpha_{5th/3rd}$, $\beta_{5th/3rd}$, $R_{3rd/1st}(0, \xi_0)$, and $R_{5th/3rd}(0, \xi_0)$ as a function of H_{ac}/T , shown in Fig. S2 within the Supplemental Material [56], are fitted by $A(H_{ac}/T)^B + C$ for the description of ξ_0 dependence. Moreover, the harmonic ratios show monotonous functions on $\omega\tau_B$ and ξ_0 , meaning that Eq. (3) has a unique solution for $\omega\tau_B$ and ξ_0 using the measured values of $R_{3rd/1st}$ and $R_{5th/3rd}$. Therefore, the solution of Eq. (3) allows one to independently calculate $\omega\tau_B$ and ξ_0 and, consequently,

determine temperature and viscosity simultaneously for the given MNP magnetic moment, m .

C. Temperature-dependent harmonic ratio

According to the Bloch law, the saturation magnetization, M_s , depends on temperature, resulting in a temperature-dependent magnetic moment, $m = M_s V_c$, with the MNP core volume V_c . Thus, to calculate the temperature, T , from $\xi_0 = \mu_0 m H_{ac} / (k_B T)$, the temperature-dependent magnetic moment, m , should be determined in advance. Here, we investigate the temperature-dependent magnetic moment, m , for the MNP sample with $c_{\text{glycerol}} = 0.0\%$. The harmonic ratios $R_{3rd/1st}$ and $R_{5th/3rd}$ are measured in an 8-mT ac magnetic field with different frequencies at different temperatures ranging from about 310 to 325 K.

Figures 2(a) and 2(b) show that $R_{3rd/1st}$ decreases whereas $R_{5th/3rd}$ increases with increasing temperature in different frequencies of ac magnetic fields. With increasing temperature, $\omega\tau_B$ decreases, resulting in an increase

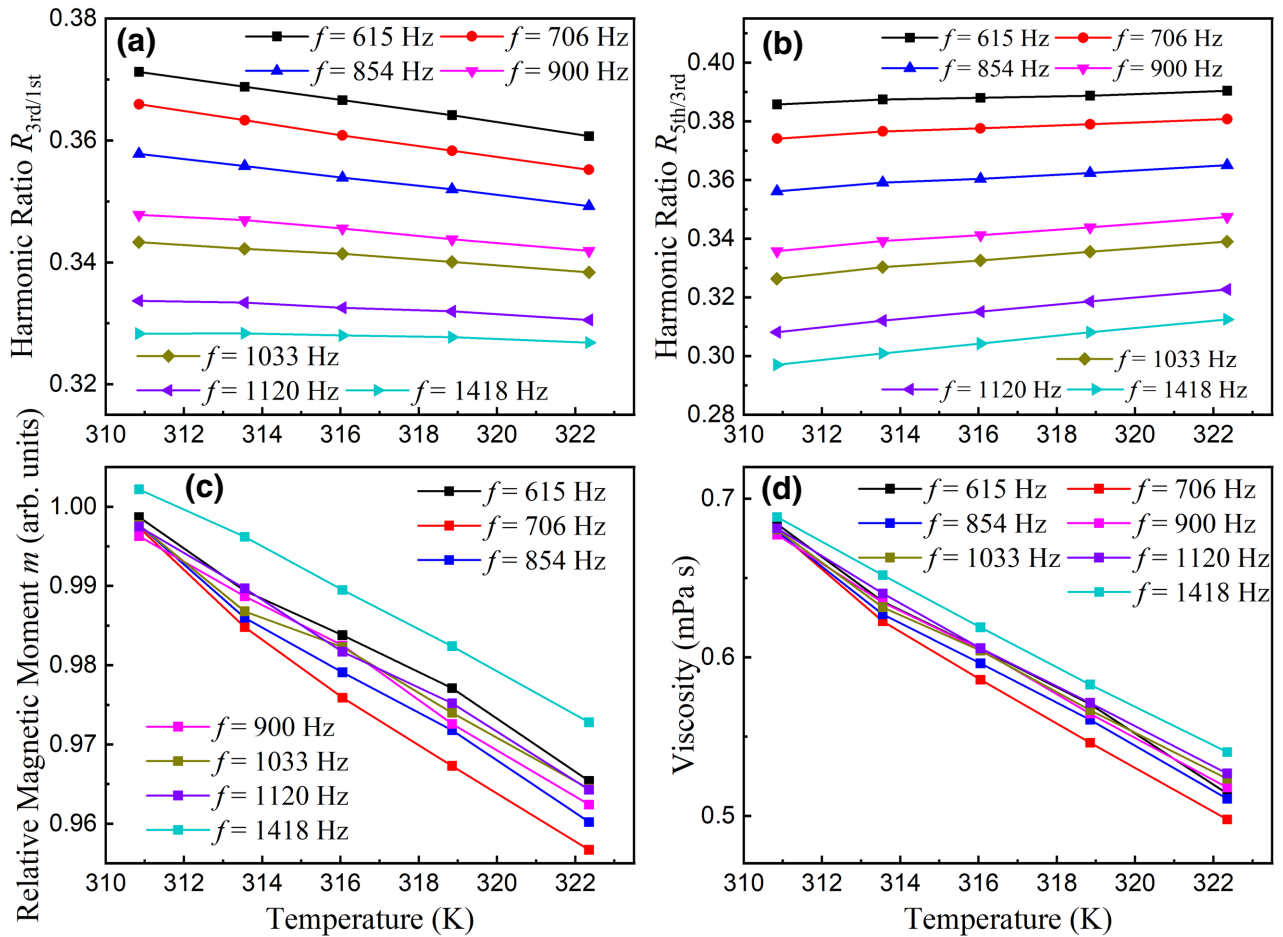


FIG. 2. Measured temperature-dependent harmonic ratios of $R_{3rd/1st}$ (a) and $R_{5th/3rd}$ (b) in different frequencies of ac magnetic fields with an amplitude of 8 mT. (c),(d) Calculated temperature-dependent relative magnetic moments in different frequencies of ac magnetic fields with an amplitude of 8 mT. Symbols are experimental results, whereas solid lines are guides to the eye.

in $R_{3rd/1st}$ and $R_{5th/3rd}$, whereas ξ_0 decreases, leading to a decrease in $R_{3rd/1st}$ and $R_{5th/3rd}$. The dependence of $R_{3rd/1st}$ and $R_{5th/3rd}$ on temperature is determined by a trade-off between $\omega\tau_B$ and ξ_0 . With the measured harmonic ratios, $R_{3rd/1st}$ and $R_{5th/3rd}$, at different temperatures, the parameters ξ_0 and $\omega\tau_B$ can be calculated with the phenomenological model of Eq. (3) and the calibrated parameters shown in Fig. S2 within the Supplemental Material [56]. For a given temperature, the magnetic moment, m , relative to that at 37.3 °C, where the free parameters in Eq. (3) are measured, is calculated, as shown in Fig. 2(c). In addition, the viscosity is calculated from $\omega\tau_B$ with the given water viscosity at 37.3 °C, as shown in Fig. 2(d). Figures 2(c) and 2(d) show that the measured magnetic moment and viscosity versus temperature curves at different frequencies collapse into single curves with some random scattering but without significant systematic changes. Some minor systematic deviation of the curve at $f_0=1418$ Hz (less than 1%) might result from the fitting difference between the phenomenological model and the experimental results and the measurement uncertainty and stability of the SMPS. Nevertheless, it means that the proposed approach allows the determination of ξ_0 and $\omega\tau_B$ independent of frequency (Brownian relaxation). Here, the temperature-dependent magnetic moment is used to determine the temperature from ξ_0 . Notably, there is no need to use the temperature-dependent viscosity shown in Fig. 2(d) to determine viscosity from $\tau_B = 3\eta V_h/(k_B T)$, since the hydrodynamic volume, V_h , can be assumed to be independent of temperature.

D. Temperature and viscosity imaging

Phantom experiments are performed at different temperatures to demonstrate the feasibility of the proposed approach for simultaneous imaging of concentration, temperature, and viscosity. The applied ac magnetic field has a constant amplitude of 8 mT and different frequencies of 615, 854, 1033, and 1418 Hz. Figure 3(a) shows a photograph of the three-line phantom, filled with three MNP samples of different viscosity. The individual MNP sample at each line can be heated by passing through temperature-controlled water via a pump for temperature imaging. A fiber-optic thermometer is placed beside each line sample (with a distance in the y direction of about 0.25 mm) for the independent temperature measurement of the given line. In principle, the temperatures of the MNP sample in the x direction are identical, whereas those in the y direction are different due to heat dissipation. The temperature profile of the phantom depends on which tube is passed by heated water. Figures 3(b)–3(d) show the images of the measured harmonics M_1 , M_3 , and M_5 at 615 Hz at room temperature (about 295 K). Each of the harmonic amplitudes can simply be transferred to visualize the spatial distribution of the MNP concentration.

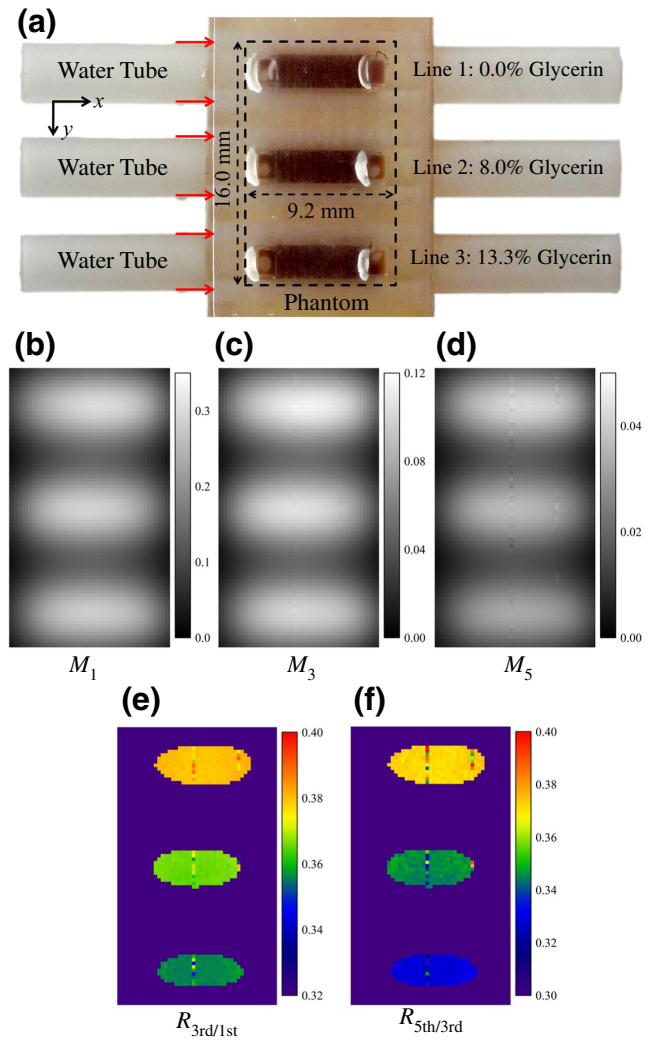


FIG. 3. (a) Photograph of phantom; images of first harmonic, M_1 (b), third harmonic, M_3 (c), and fifth harmonic, M_5 (d), in an ac magnetic field with a frequency of 615 Hz at room temperature (295 K). Red arrows in (a) represent the positions where the temperature of the MNP samples are measured by a fiber-optic thermometer. $R_{3rd/1st}$ (e) and $R_{5th/3rd}$ (f) images calculated from images of M_1 , M_3 , and M_5 .

The harmonic ratio images of $R_{3rd/1st}$ and $R_{5th/3rd}$ are calculated from the measured images of M_1 , M_3 , and M_5 . Notably, the proposed approach employs the MNPs to act as nanosensors for the measurements of temperature and viscosity. At a specific position, where there are no MNPs, the proposed approach does not allow the measurements of temperature and viscosity. Thus, a threshold, δ with a value of 0.35, relative to the maximum intensity of the first harmonic, is applied to calculate the images of $R_{3rd/1st}$ and $R_{5th/3rd}$. Previous studies have demonstrated that deconvolution of the measured harmonics images provides a higher spatial resolution but also results in some artifacts on the temperatures. Thus, in this paper, the temperature and viscosity images, as shown in Figs. 3(e) and 3(f), are

obtained with the measured harmonic ratio images without deconvolution.

From the images of $R_{3rd/1st}$ and $R_{5th/3rd}$, temperature and viscosity imaging is realized with the phenomenological model of Eq. (3). Figure 4 shows the measured temperature and viscosity images. The first (third) column in Fig. 4 shows the temperature (viscosity) images for different heating positions, i.e., “no heat,” “heat line 1,” “heat

line 2,” and “heat line 3” at $H_{ac}=8$ mT and $f = 615$ Hz. The temperature and viscosity images at $f = 854, 1033,$ and 1418 Hz are presented in Figs. S3–S5 within the Supplemental Material [56]. The second (forth) column in Fig. 4 shows the x -direction average temperature (viscosity) versus y position curves in different frequencies of ac magnetic fields. Figures 4(a) and 4(b) show that without any external heating (no heat) the measured temperature

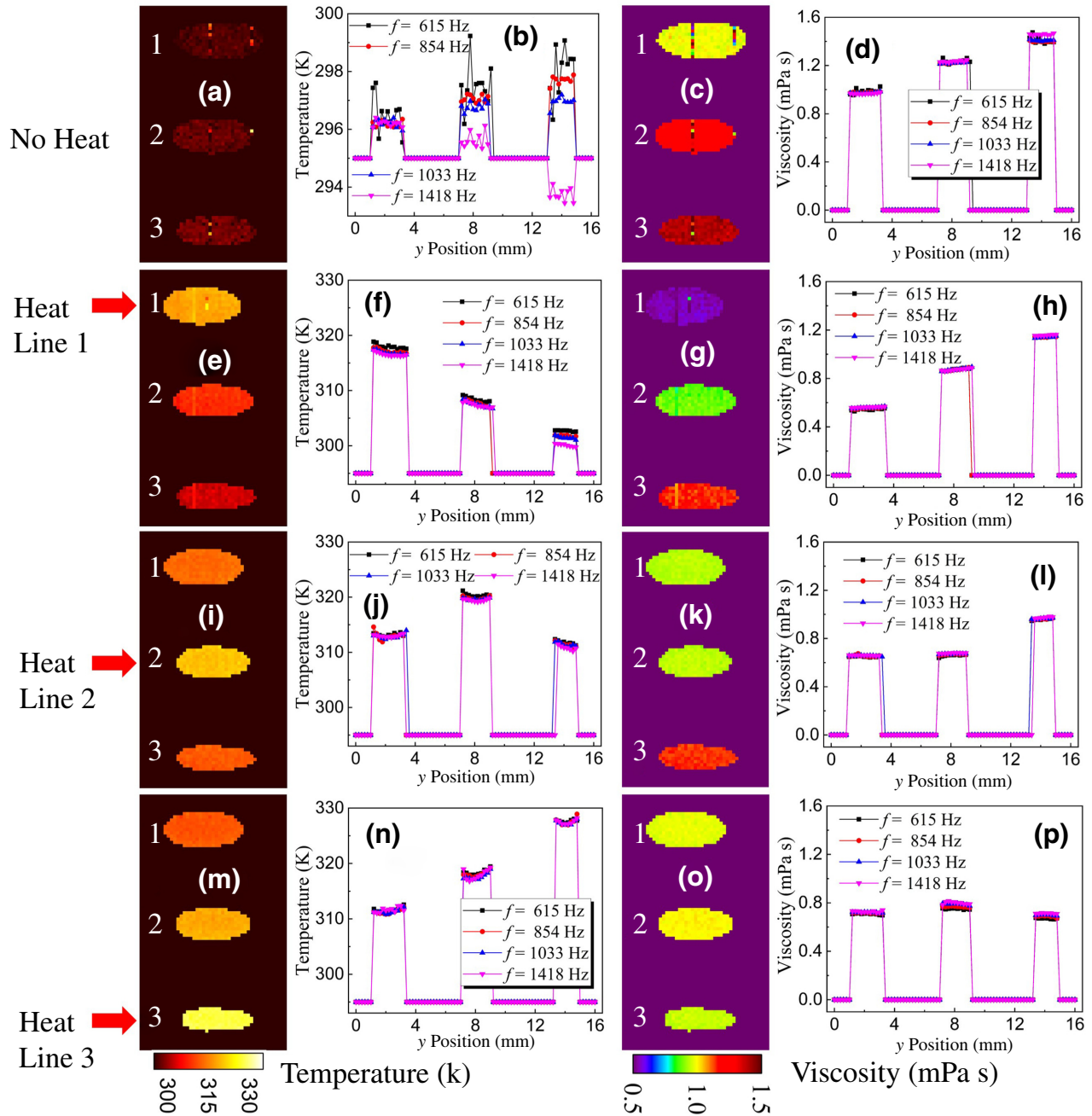


FIG. 4. Experimental results of temperature and viscosity images of the three-line phantom. Unit of temperature (viscosity) is K (mPa s). First (third) column shows 2D temperature (viscosity) images in an ac magnetic field with an amplitude of 8 mT and frequency of 615 Hz. Second (forth) column shows temperature (viscosity) versus y position curves in different frequencies of ac magnetic fields with an amplitude of 8 mT. Symbols in the curves are experimental data, whereas solid lines are a guide to the eye.

image does not show a significant temperature gradient. The viscosity images of the three-line samples displayed in Figs. 4(c) and 4(d) show that the viscosity of the MNP sample increases from line 1 to line 3 due to a higher percentage of glycerol. Figures 4(e) and 4(f) indicate that with heating at line 1 (heat line 1) the temperature image shows a significant temperature gradient of the three-line phantom with the highest-temperature area at line 1. In addition, the temperature gradually decreases from line 1 to line 3 due to heat dissipation, which is expected due to the water tube placed at line 1. In addition, the water-tube position is changed to heat different MNP samples, as shown in Fig. 4. The highest-temperature area consequently changes from line 1 to line 3, which correlates very well with the water-tube position (heating position). The viscosity images do not show the highest viscosity at line 3 for different heating positions due to the decrease in viscosity with increasing temperature. For example, with heating at line 3 (heat line 3), the MNP sample of line 3 has the highest

temperature, compared to the other two lines of MNP samples. It means that the sample viscosity of the MNP sample at line 3 decreases more significantly than that of the other two samples. Moreover, the second and fourth columns in Fig. 4 show that the measured temperatures and viscosities in different frequencies of ac magnetic fields do not show significant variations. Scattering in the measured temperature and viscosity images is caused by external interference and the system's instability.

The standard deviation and average of the measured temperatures, T_{MNP} (viscosity, η_{MNP}), along a line in the x direction (at the same y position) are calculated to analyze the temperature (viscosity) resolution and deviation from references. Figures 5(a) and 5(b) show the measured temperature and viscosity resolutions at $f = 615$ Hz, respectively. They indicate that the temperature resolution is about 1 K, while the viscosity resolution is about 0.03 mPa.s. Figures S6–S8 within the Supplemental Material [56] show the temperature

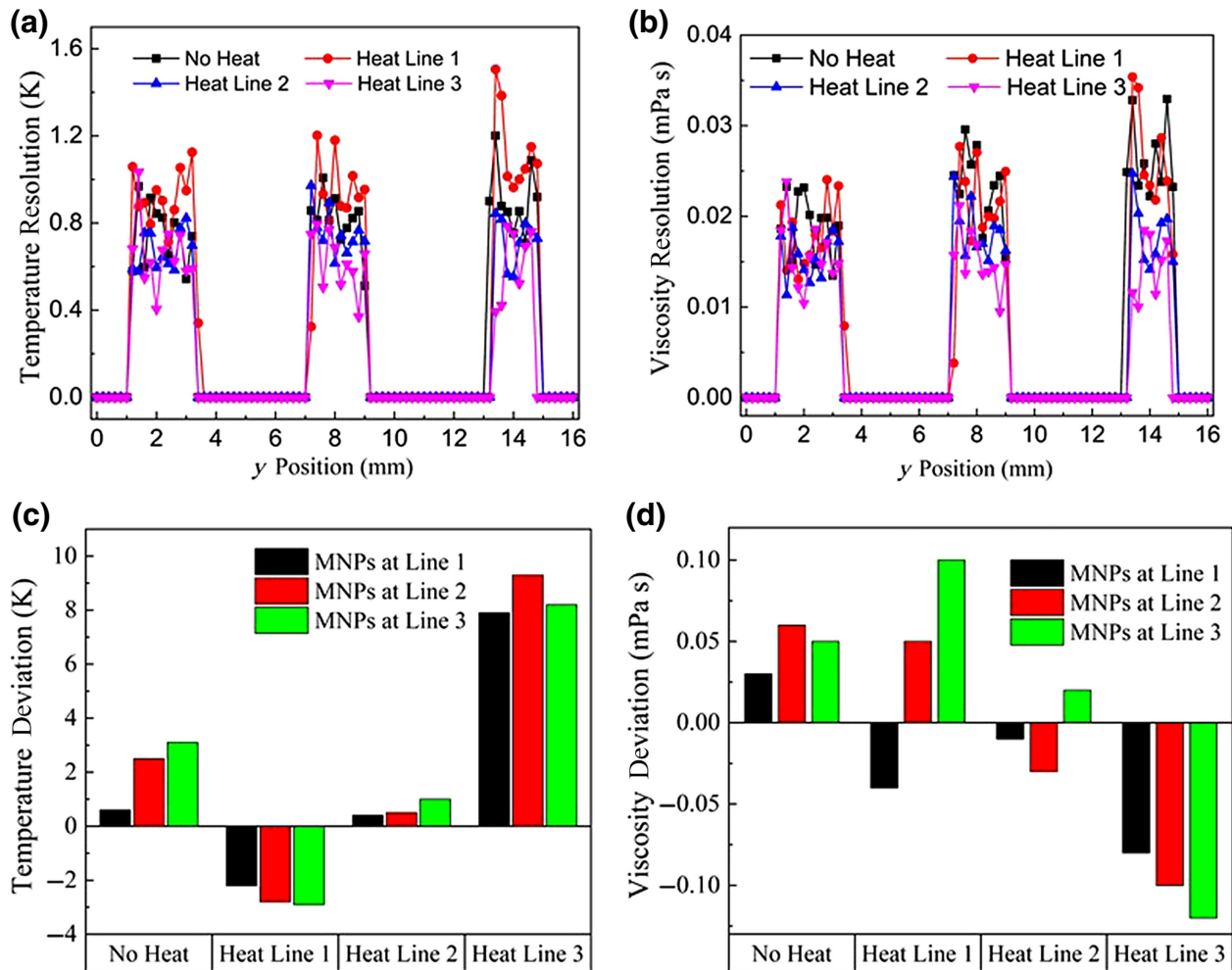


FIG. 5. (a),(b) Temperature and viscosity resolutions versus y position for different heating positions at 615 Hz. Symbols are experimental results, whereas solid lines are guides to the eye. (c),(d) Temperature and viscosity deviations compared to references.

resolution of about 0.7 K and viscosity resolution of about 0.02 mPa s at higher frequencies, which are slightly better than those at $f = 615$ Hz. It may be caused by a better signal-to-noise ratio at higher frequencies. To evaluate the measured deviations in temperature and viscosity, the temperature, T_{optic} , measured with a fiber-optic thermometer and the theoretical viscosity, η_{theory} , are used as references. Figures 5(c) and 5(d) show the temperature deviation, $\Delta T = T_{\text{MNP}} - T_{\text{optic}}$, and the viscosity deviation $\Delta\eta = \eta_{\text{MNP}} - \eta_{\text{theory}}$, respectively. At no heat, heat line 1, and heat line 2, the maximum deviation in temperature (viscosity) is 3.1 K (0.1 mPa s), whereas, at heat line 3, the maximum deviation in temperature (viscosity) is 9.3 K (0.12 mPa s).

IV. DISCUSSION

The proposed approach employs the dynamic magnetization of MNPs dominated by Brownian relaxation to realize simultaneous imaging of MNP concentration, temperature, and viscosity. The solution of the FPE indicates that dynamic magnetization of the MNPs dominated by Brownian relaxation depends only on three free parameters of c , $\omega\tau_B = 2\pi f\eta V_h/(k_B T)$, and $\xi_0 = \mu_0 m H_{\text{ac}}/(k_B T)$. It means that $R_{3\text{rd}/1\text{st}}$ and $R_{5\text{th}/3\text{rd}}$ are dependent on $\omega\tau_B$ and ξ_0 but independent of c . Furthermore, $R_{3\text{rd}/1\text{st}}$ and $R_{5\text{th}/3\text{rd}}$ versus $f\eta$ curves of the MNP samples with different viscosities at a constant temperature should collapse into a single curve in an ac magnetic field with a constant amplitude, as verified by our experimental results (see Fig. 1). Thus, the viscosity and frequency have the same effects on MNP magnetization and the harmonic ratio. Similarly, the amplitude, H_{ac} , and temperature have similar effects on MNP magnetization and the harmonic ratio, but not on the temperature-dependent viscosity. The proposed phenomenological model of Eq. (3) decouples the effects of $\omega\tau_B$ and ξ_0 on the harmonic ratios, which has the same effect as the proposed model in Ref. [50]. It indicates that $R_{3\text{rd}/1\text{st}}$ and $R_{5\text{th}/3\text{rd}}$ are monotonous functions of $\omega\tau_B$ and ξ_0 , as demonstrated by our experimental results (see Fig. 2). It means that Eqs. (1a) and (1b) have a unique solution for temperature and viscosity measurements for the measured $R_{3\text{rd}/1\text{st}}$ and $R_{5\text{th}/3\text{rd}}$ values. Consequently, MNP-concentration imaging is realized by the measured images of the harmonic amplitude, M_i , while temperature and viscosity imaging are achieved by the imaging of the harmonic ratios of $R_{3\text{rd}/1\text{st}}$ and $R_{5\text{th}/3\text{rd}}$ with the SMPS. Thus, the proposed approach independently visualizes the spatial distributions of temperature and viscosity determined from the measured images of $R_{3\text{rd}/1\text{st}}$ and $R_{5\text{th}/3\text{rd}}$ independent of frequency. Moreover, the proposed approach allows one to measure the temperature-dependent viscosity.

However, the measured temperature and viscosity images show some deviations from the temperature measured by the fiber-optic thermometer and the

theoretical viscosity, respectively. Without external heating, the maximum absolute deviation from the nominal temperature, ΔT , is 3.1 K, while the maximum absolute deviation of the viscosity, $\Delta\eta$, is about 0.1 mPa s. With heating line 1 and line 2, the deviations in temperature and viscosity are similar to those without any heating. With external heating at line 3, the measured temperature has a significant deviation of 9.3 K, while the measured viscosity has a deviation of about 0.12 mPa s. Notably, in spite of the maximum temperature deviation of 9.3 K and the viscosity deviation of 0.12 mPa s, the temperature and viscosity resolutions are about 1 K and 0.03 mPa s, respectively. Moreover, Fig. S9 within the Supplemental Material [56] shows the measured viscosity versus temperature curves of the MNP suspensions at different heating positions. It indicates that with increasing temperature the viscosity decreases, which qualitatively fits with theory. Therefore, we believe that these deviations are mainly dominated by systematic errors.

The deviations in temperature and viscosity from the reference values may result from several sources, including the reference values of temperature and viscosity and the proposed phenomenological model. First, the reference values of temperature (measured by fiber-optic thermometer) and viscosity (calculated from theory) may also differ from the real temperature and viscosity of the MNP sample. In experiments, the fiber-optic thermometer is not directly placed in the MNP suspension for temperature measurements. Second, the measured temperature and viscosity significantly depend on the calibrated parameters in Eq. (3). A deviation of 1% between the phenomenological model of Eq. (3) and experimental data may result in ΔT of about 3 K and $\Delta\eta$ of about 0.01 mPa s. Finally, the influence of Néel relaxation on the dynamic magnetization of the MNPs is completely ignored in the phenomenological model. Thus, the proposed approach is only valid for Brownian-relaxation-dominated MNPs. With a Néel-relaxation contribution to MNP magnetization, the ratio of anisotropy energy to thermal energy plays a significant role in the MNP harmonics, which breaks the validation of the proposed approach. The Néel contribution may come from some portions of smaller MNPs in the experimental sample and the intra-potential-well contribution of the larger MNPs [58,59]. Furthermore, these Néel contributions become more significant with increasing viscosity and temperature. It may explain that with heating line 3 the deviations in temperature and viscosity are more significant, which also qualitatively agrees with published results [50]. Although the maximum deviation in temperature (viscosity) is about 9.3 K (0.12 mPa s) with heating line 3, the measured temperature (viscosity) can very well distinguish the temperatures of the MNP samples at line 1 and line 2 with a temperature difference of 6 K (0.05 mPa s). It demonstrates that the maximum deviations mainly result from systematic error.

The measurement resolutions of temperature and viscosity can be improved by repeated measurements, while the measurement accuracies can be improved by the use of MNPs purely dominated by Brownian relaxation. Here, the measurement time for each point of temperature and viscosity is 0.02 s, allowing temperature and viscosity resolutions of about 1 K and 0.03 mPa s, respectively. They can be further improved with a longer measurement time and an excitation magnetic field with a higher amplitude and frequency. The use of MNPs with only Brownian relaxation might significantly improve the systematic errors in temperature and viscosity. The experimental samples of SHP-25 with iron-oxide nanoparticles are proven to have some Néel-relaxation contributions. We believe that further investigation of the synthesis of iron-oxide nanoparticles by chemists and/or materials scientists will significantly improve their applications in multiparametric imaging.

The application of the present approach in personalized medicine for the imaging of MNP concentration, temperature, and viscosity significantly depends on the contribution of Brownian and Néel relaxations to MNP dynamic magnetization. Here, the studied viscosity from 0.69 to 0.95 mPa s at 37 °C is slightly below that of blood-plasma viscosity (1.2–1.3 mPa s at 37 °C). A higher viscosity may increase the contribution of Néel relaxation to MNP dynamic magnetization, thus worsening the temperature and viscosity measurement accuracy. In addition, small MNPs, e.g., smaller than 15 nm, are preferred in personalized medicine for several reasons, e.g., protein-corona effect and macrophage uptake [60,61]. For smaller MNPs, Néel relaxation may play a significant role in their dynamic magnetization due to a smaller core volume, causing the present approach not to be applicable. However, this is not always the case, since Néel relaxation mainly depends on the magnetic anisotropy energy, which is the product of the magnetic anisotropy constant and the MNP core volume, not just the MNP core volume. With an extremely large magnetic anisotropy constant, smaller MNPs, with sizes of 15 nm, may have extremely high magnetic anisotropy energy, showing a very long Néel-relaxation time. Thus, the magnetic easy axes of the MNPs cannot rotate via Néel relaxation but via a Brownian-relaxation mechanism. Therefore, the MNP's dynamic magnetization is mainly dominated by the Brownian-relaxation mechanism. Notably, this behavior also depends on the chemical formulas of different types of magnetic ions, since the formulation of the magnetic ions affects the magnetic anisotropy constant. The magnetic anisotropy of MNPs can be enhanced during synthesis with different methods, e.g., particle doping, formation of alloys, and surface modification [62–64]. With different formulations of magnetic ions, e.g., Co, during synthesis, the magnetic anisotropy energy of the MNPs can be significantly increased. Thus, the MNP's dynamic magnetization can be

mainly or even purely contributed to by Brownian relaxation. In this case, the proposed approach can be applicable to a high-viscosity environment, e.g., for blood or plasma viscosity imaging, while the temperature and viscosity measurement accuracy can be significantly improved. In addition, octahedral-shaped MNPs are demonstrated to have a larger magnetic anisotropy than that of spherical MNPs [65]. Nevertheless, several different MNPs larger than 15 nm, e.g., Resovist, vivoTrax from Magnetic Insight Inc. (Alameda, USA), and perimag from micromod Partikeltechnologie GmbH (Rostock, Germany), show great promise in biomedical applications, including cardiovascular and inflammation imaging, cancer detection, magnetic hyperthermia, and stem- or immune-cell tracking [66–70]. Another important issue is the delivery of MNPs to a target tissue. Due to their magnetic properties, a gradient magnetic field can be applied to enhance the accumulation of MNPs in a specific target tissue for disease diagnostics and therapy [71,72]. Therefore, in principle, the present approach should be applicable to personalized medicine by selecting and synthesizing specific MNPs.

In addition, the temperature accuracy of the present approach and the measurement system is also important for real applications of the current approach in personalized medicine. The current approach allows a temperature measurement accuracy of about 9 K, which mainly comes from the systematic errors caused by Néel relaxation, as discussed above. In some applications that only require the monitoring of temperature changes, the current approach can still be applicable, due to a temperature resolution of about 1 K. With the requirements for absolute temperature measurement, the current approach is not applicable. In this case, MNPs with purely Brownian relaxation should be specifically selected. In addition, to improve temperature accuracy, MNPs with Néel-relaxation domination can be used to exclude the influence of viscosity on their dynamic magnetization. However, this will result in a loss of the feasibility of viscosity measurement. A combination of two different MNP systems with either purely Brownian relaxation or Néel relaxation might be a good choice in this regard to measure temperature and viscosity. Notably, the proposed approach mainly demonstrates the feasibility of multiparametric imaging of MNP concentration, temperature, and viscosity. For real applications, further studies on MNP synthesis and modeling of the dynamic magnetization of MNPs are required. The current measurement system, the SMPS, based on mechanical scanning allows for the two-dimensional imaging of MNPs. In principle, it does not have any depth limitations due to the penetration of magnetic fields. However, with increasing depth, both the spatial resolution and the sensitivity get worse. For the application of the current approach in the human body, the SMPS probably allows the detection of MNPs at a depth of a few centimeters, but not the whole body with a large volume. The presented approach mainly demonstrates the

feasibility of multiparametric imaging, including MNP concentration, temperature, and viscosity, by using the proposed phenomenological model. For real applications in human bodies, the MNPs and the measurement system, as well as the physical models, should be further improved. For real applications in the human body, a 3D MPI scanner with gradient magnetic fields for spatial encoding is preferred [73].

V. CONCLUSION

This paper reports on an approach to the simultaneous imaging of MNP concentration, temperature, and viscosity. A phenomenological model based on the FPE is proposed to investigate the effects of the relaxation parameter, $\omega\tau_B$, and the Langevin parameter, ξ_0 , on the harmonic ratios $R_{3rd/1st}$ and $R_{5th/3rd}$, which is verified by our experimental results. A three-line phantom is filled with different-viscosity MNP samples for experiments at different spatial distributions of temperature. The images of harmonic amplitude are simply converted to realize MNP-concentration imaging, whereas the images of $R_{3rd/1st}$ and $R_{5th/3rd}$ are calculated to realize temperature and viscosity imaging by applying the phenomenological model. Our experimental results demonstrate the feasibility of the proposed approach for the simultaneous imaging of MNP concentration, temperature, and viscosity. We envisage that the proposed approach is of great interest and significance not only for the extension of MPI to multiparametric MPI but also to biomedicine for disease diagnostics and therapy. We believe that the proposed approach will provide tools for the *in vivo* tracking of substances, e.g., gene, stem cells, and drugs, and act as sensors for the measurements of local microenvironmental parameters, which will make a remarkable contribution to precision medicine.

ACKNOWLEDGMENTS

Financial support from the National Key R&D Program of China under Grant No. 2019YFB1309700, the German Research Foundation (DFG) under Grant No. ZH 782/1-1, and the Alexander von Humboldt Foundation are gratefully acknowledged.

-
- [1] S. Gaballa, N. Palmisiano, O. Alpdogan, M. Carabasi, J. Filicko-O'Hara, M. Kasner, W. K. Kraft, B. Leiby, U. Martinez-Outschoorn, and W. O'Hara, A two-step haploidentical versus a two-step matched related allogeneic myeloablative peripheral blood stem cell transplantation, *Biol. Blood Marrow Transplant.* **22**, 141 (2016).
- [2] R. S. Mahla, Stem cells applications in regenerative medicine and disease therapeutics, *Int. J. Cell Biol.* **2016**, 6940283 (2016).

- [3] J. H. Park, T. Spitzer, and D. J. Kuter, Successful treatment of pure red cell aplasia with autologous stem cell transplantation, *Am. J. Hematol.* **82**, 812 (2007).
- [4] A. Trafton, Tumor targeted using tiny gold particles, MIT Tech Talk **53**, 1 (2009).
- [5] Y. H. Bae and K. Park, Targeted drug delivery to tumors: Myths, reality and possibility, *J. Control. Release* **153**, 198 (2011).
- [6] S. M. Cromer Berman, P. Walczak, and J. W. Bulte, Tracking stem cells using magnetic nanoparticles, *Wiley Interdiscip. Rev. Nanomed. Nanobiotechnol.* **3**, 343 (2011).
- [7] A. Solanki, J. D. Kim, and K.-B. Lee, Nanotechnology for regenerative medicine: Nanomaterials for stem cell imaging, *Nanomedicine* **3**, 567 (2008).
- [8] C. S. Kumar and F. Mohammad, Magnetic nanomaterials for hyperthermia-based therapy and controlled drug delivery, *Adv. Drug Deliv. Rev.* **63**, 789 (2011).
- [9] T. D. Vreugdenburg, C. D. Willis, L. Mundy, and J. E. Hiller, A systematic review of elastography, electrical impedance scanning, and digital infrared thermography for breast cancer screening and diagnosis, *Breast Cancer Res. Treat.* **137**, 665 (2013).
- [10] R. J. DeBerardinis, J. J. Lum, G. Hatzivassiliou, and C. B. Thompson, The biology of cancer: Metabolic reprogramming fuels cell growth and proliferation, *Cell Metab.* **7**, 11 (2008).
- [11] A. E. Deatsch and B. A. Evans, Heating efficiency in magnetic nanoparticle hyperthermia, *J. Magn. Magn. Mater.* **354**, 163 (2014).
- [12] A. Jordan, R. Scholz, P. Wust, H. Fähling, and R. Felix, Magnetic fluid hyperthermia (MFH): Cancer treatment with AC magnetic field induced excitation of biocompatible superparamagnetic nanoparticles, *J. Magn. Mag. Mater.* **201**, 413 (1999).
- [13] R. E. Rosensweig, Heating magnetic fluid with alternating magnetic field, *J. Magn. Mag. Mater.* **252**, 370 (2002).
- [14] H. A. Albarqi, L. H. Wong, C. Schumann, F. Y. Sabei, T. Korzun, X. Li, M. N. Hansen, P. Dhagat, A. S. Moses, and O. Taratula, Biocompatible nanoclusters with high heating efficiency for systemically delivered magnetic hyperthermia, *ACS Nano* **13**, 6383 (2019).
- [15] D. S. Long, M. L. Smith, A. R. Pries, K. Ley, and E. R. Damiano, Microviscometry reveals reduced blood viscosity and altered shear rate and shear stress profiles in microvessels after hemodilution, *Proc. Natl. Acad. Sci.* **101**, 10060 (2004).
- [16] G. Chen, L. Zhao, Y. Liu, F. Liao, D. Han, and H. Zhou, Regulation of blood viscosity in disease prevention and treatment, *Chinese Sci. Bull.* **57**, 1946 (2012).
- [17] B. Okafor and G. MacLellan, Postoperative changes of erythrocyte sedimentation rate, plasma viscosity and C-reactive protein levels after hip surgery, *Acta Orthop. Belg.* **64**, 52 (1998).
- [18] T. Celik, S. Balta, C. Ozturk, and A. Iyisooy, Whole blood viscosity and cardiovascular diseases: A forgotten old player of the game, *Med. Princ. Pract.* **25**, 499 (2016).
- [19] S. A. Peters, M. Woodward, A. Rumley, H. D. Tunstall-Pedoe, and G. D. Lowe, Plasma and blood viscosity in the prediction of cardiovascular disease and mortality in the scottish heart health extended cohort study, *Eur. J. Prev. Cardiol.* **24**, 161 (2017).

- [20] M. M. Smith, P. C. Chen, C.-S. Li, S. Ramanujam, and A. T. Cheung, Whole blood viscosity and microvascular abnormalities in Alzheimer's disease, *Clin. Hemorheol. Microcirc.* **41**, 229 (2009).
- [21] B. Gleich and J. Weizenecker, Tomographic imaging using the nonlinear response of magnetic particles, *Nature* **435**, 1214 (2005).
- [22] J. Weizenecker, B. Gleich, and J. Borgert, Magnetic particle imaging using a field free line, *J. Physics D: Appl. Phys.* **41**, 105009 (2008).
- [23] P. W. Goodwill and S. M. Conolly, The X-space formulation of the magnetic particle imaging process: 1-D signal, resolution, bandwidth, SNR, SAR, and magnetostimulation, *IEEE Trans. Med. Imaging* **29**, 1851 (2010).
- [24] M. Schilling, F. Ludwig, C. Kuhlmann, and T. Wawrzik, Magnetic particle imaging scanner with 10-kHz drive-field frequency, *Biomedizinische Technik. Biomedical Eng.* **58**, 557 (2013).
- [25] S. Pi, W. Liu, and T. Jiang, Real-time and quantitative isotropic spatial resolution susceptibility imaging for magnetic nanoparticles, *Meas. Sci. Technol.* **29**, 035402 (2018).
- [26] H. Richter, M. Kettering, F. Wiekhorst, U. Steinhoff, I. Hilger, and L. Trahms, Magnetorelaxometry for localization and quantification of magnetic nanoparticles for thermal ablation studies, *Phys. Med. Biol.* **55**, 623 (2010).
- [27] J. Zhong, M. Schilling, and F. Ludwig, Magnetic nanoparticle temperature imaging with a scanning magnetic particle spectrometer, *Meas. Sci. Technol.* **29**, 115903 (2018).
- [28] P. Vogel, M. A. Rückert, P. Klauer, W. H. Kullmann, P. M. Jakob, and V. C. Behr, Traveling wave magnetic particle imaging, *IEEE Trans. Med. Imaging* **33**, 400 (2013).
- [29] J. Weizenecker, B. Gleich, J. Rahmer, H. Dahnke, and J. Borgert, Three-dimensional real-time in vivo magnetic particle imaging, *Phys. Med. Biol.* **54**, L1 (2009).
- [30] H. Arami, E. Teeman, A. Troksa, H. Bradshaw, K. Saatchi, A. Tomitaka, S. S. Gambhir, U. O. Häfeli, D. Liggitt, and K. M. Krishnan, Tomographic magnetic particle imaging of cancer targeted nanoparticles, *Nanoscale* **9**, 18723 (2017).
- [31] M. Graeser, T. Knopp, P. Szwargulski, T. Friedrich, A. von Gladiss, M. Kaul, K. M. Krishnan, H. Itrich, G. Adam, and T. M. Buzug, Towards picogram detection of superparamagnetic iron-oxide particles using a gradiometric receive coil, *Sci. Rep.* **7**, 6872 (2017).
- [32] Z. W. Tay, D. Hensley, J. Ma, P. Chandrasekharan, B. Zheng, P. Goodwill, and S. Conolly, Pulsed excitation in magnetic particle imaging, *IEEE Trans. Med. Imaging* **38**, 2389 (2019).
- [33] V. L. Calero-DdelC, D. I. Santiago-Quiñonez, and C. Rinaldi, Quantitative nanoscale viscosity measurements using magnetic nanoparticles and SQUID AC susceptibility measurements, *Soft Matter* **7**, 4497 (2011).
- [34] S. Draack, N. Lucht, H. Remmer, M. Martens, B. Fischer, M. Schilling, F. Ludwig, and T. Viereck, Multiparametric magnetic particle spectroscopy of CoFe_2O_4 nanoparticles in viscous media, *J. Phys. Chem. C* **123**, 6787 (2019).
- [35] H. Remmer, J. Dieckhoff, A. Tschöpe, E. Roeben, A. M. Schmidt, and F. Ludwig, Dynamics of CoFe_2O_4 single-core nanoparticles in viscoelastic media, *Phys. Procedia* **75**, 1150 (2015).
- [36] J. B. Weaver and E. Kuehlert, Measurement of magnetic nanoparticle relaxation time, *Med. Phys.* **39**, 2765 (2012).
- [37] M. Utkur, Y. Muslu, and E. U. Saritas, Relaxation-based viscosity mapping for magnetic particle imaging, *Phys. Med. Biol.* **62**, 3422 (2017).
- [38] K. Wu, D. Su, R. Saha, J. Liu, V. K. Chugh, and J.-P. Wang, Magnetic particle spectroscopy: A short review of applications using magnetic nanoparticles, *ACS Appl. Nano Mater.* **3**, 4972 (2020).
- [39] K. Wu, K. Schliep, X. Zhang, J. Liu, B. Ma, and J. P. Wang, Characterizing physical properties of superparamagnetic nanoparticles in liquid phase using Brownian relaxation, *Small* **13**, 1604135 (2017).
- [40] J. Rahmer, A. Halkola, B. Gleich, I. Schmale, and J. Borgert, First experimental evidence of the feasibility of multi-color magnetic particle imaging, *Phys. Med. Biol.* **60**, 1775 (2015).
- [41] M. Möddel, C. Meins, J. Dieckhoff, and T. Knopp, Viscosity quantification using multi-contrast magnetic particle imaging, *New J. Phys.* **20**, 083001 (2018).
- [42] M. Utkur, Y. Muslu, and E. Saritas, Relaxation-based color magnetic particle imaging for viscosity mapping, *Appl. Phys. Lett.* **115**, 152403 (2019).
- [43] J. Zhong, W. Liu, Z. Du, P. C. de Morais, Q. Xiang, and Q. Xie, A noninvasive, remote and precise method for temperature and concentration estimation using magnetic nanoparticles, *Nanotechnology* **23**, 075703 (2012).
- [44] J. Zhong, W. Liu, L. Kong, and P. C. Morais, A new approach for highly accurate, remote temperature probing using magnetic nanoparticles, *Sci. Rep.* **4**, 6338 (2014).
- [45] J. Zhong, W. Liu, L. Jiang, M. Yang, and P. C. Morais, Real-time magnetic nanothermometry: The use of magnetization of magnetic nanoparticles assessed under low frequency triangle-wave magnetic fields, *Rev. Sci. Instrum.* **85**, 094905 (2014).
- [46] M. Zhou, J. Zhong, W. Liu, Z. Du, Z. Huang, M. Yang, and P. C. Morais, Study of magnetic nanoparticle spectrum for magnetic nanothermometry, *IEEE Trans. Magn.* **51**, 6101006 (2015).
- [47] J. B. Weaver, A. M. Rauwerdink, and E. W. Hansen, Magnetic nanoparticle temperature estimation, *Med. Phys.* **36**, 1822 (2009).
- [48] J. Zhong, J. Dieckhoff, M. Schilling, and F. Ludwig, Influence of static magnetic field strength on the temperature resolution of a magnetic nanoparticle thermometer, *J. Appl. Phys.* **120**, 143902 (2016).
- [49] L. He, W. Liu, Q. Xie, S. Pi, and P. Morais, A fast and remote magnetonanothermometry for a liquid environment, *Meas. Sci. Technol.* **27**, 025901 (2015).
- [50] J. Zhong, M. Schilling, and F. Ludwig, Magnetic nanoparticle thermometry independent of Brownian relaxation, *J. Phys. D: Appl. Phys.* **51**, 015001 (2017).
- [51] C. Stehning, B. Gleich, and J. Rahmer, Simultaneous magnetic particle imaging (MPI) and temperature mapping using multi-color MPI, *Int J Magn Part Imaging* **2**, 1612001 (2016).
- [52] J. Zhong, M. Schilling, and F. Ludwig, Excitation frequency dependence of temperature resolution in magnetic

- nanoparticle temperature imaging with a scanning magnetic particle spectrometer, *J. Magn. Magn. Mater.* **471**, 340 (2019).
- [53] H. Vogel, The temperature dependence law of the viscosity of fluids, *Phys. Z* **22**, 645 (1921).
- [54] T. Yoshida and K. Enpuku, Simulation and quantitative clarification of AC susceptibility of magnetic fluid in non-linear Brownian relaxation region, *Jpn. J. Appl. Phys.* **48**, 127002 (2009).
- [55] M. A. Martens, R. J. Deissler, Y. Wu, L. Bauer, Z. Yao, R. Brown, and M. Griswold, Modeling the Brownian relaxation of nanoparticle ferrofluids: Comparison with experiment, *Med. Phys.* **40**, 022303 (2013).
- [56] See the Supplemental Material at <http://link.aps.org/supplemental/10.1103/PhysRevApplied.16.054005> for additional detailed data, including ACS spectra, fitted parameters, phantom images, and temperature-dependent viscosities.
- [57] N.-S. Cheng, Formula for the viscosity of a glycerol–water mixture, *Ind. Eng. Chem.* **47**, 3285 (2008).
- [58] F. Ludwig, C. Balceris, and C. Johansson, The anisotropy of the ac susceptibility of immobilized magnetic nanoparticles—The influence of intra-potential-well contribution on the ac susceptibility spectrum, *IEEE Trans. Magn.* **53**, 6101004 (2017).
- [59] P. Svedlindh, T. Jonsson, and J. García-Palacios, Intra-potential-well contribution to the AC susceptibility of a noninteracting nano-sized magnetic particle system, *J. Magn. Magn. Mater.* **169**, 323 (1997).
- [60] K. Partikel, R. Korte, N. C. Stein, D. Mulac, F. C. Herrmann, H.-U. Humpf, and K. Langer, Effect of nanoparticle size and PEGylation on the protein corona of PLGA nanoparticles, *Eur. J. Pharm. Biopharm.* **141**, 70 (2019).
- [61] R. García-Álvarez, M. Hadjidemetriou, A. Sánchez-Iglesias, L. M. Liz-Marzán, and K. Kostarelos, In vivo formation of protein corona on gold nanoparticles. The effect of their size and shape, *Nanoscale* **10**, 1256 (2018).
- [62] Y. Prado, N. Daffé, A. Michel, T. Georgelin, N. Yaacoub, J.-M. Grenèche, F. Choueikani, E. Otero, P. Ohresser, M.-A. Arrio, C. Cartier-dit-Moulin, P. Saintavit, B. Fleury, V. Dupuis, L. Lisnard, and J. Fresnais, Enhancing the magnetic anisotropy of maghemite nanoparticles via the surface coordination of molecular complexes, *Nat. Commun.* **6**, 10139 (2015).
- [63] C. Vichery, I. Maurin, O. Proux, I. Kieffer, J.-L. Hazemann, R. Cortès, J.-P. Boilot, and T. Gacoin, Introduction of cobalt ions in γ -Fe₂O₃ nanoparticles by direct coprecipitation or postsynthesis adsorption: Dopant localization and magnetic anisotropy, *J. Phys. Chem. C* **117**, 19672 (2013).
- [64] J. Salafranca, J. Gazquez, N. Pérez, A. Labarta, S. T. Pantelides, S. J. Pennycook, X. Batlle, and M. Varela, Surfactant organic molecules restore magnetism in metal-oxide nanoparticle surfaces, *Nano Lett.* **12**, 2499 (2012).
- [65] H. Mamiya, H. Fukumoto, J. L. C. Huaman, K. Suzuki, H. Miyamura, and J. Balachandran, Estimation of magnetic anisotropy of individual magnetite nanoparticles for magnetic hyperthermia, *ACS Nano* **14**, 8421 (2020).
- [66] J. Haegel, J. Rahmer, B. Gleich, J. Borgert, H. Wojtczyk, N. Panagiotopoulos, T. M. Buzug, J. Barkhausen, and F. M. Vogt, Magnetic particle imaging: Visualization of instruments for cardiovascular intervention, *Radiology* **265**, 933 (2012).
- [67] D. B. Mangarova, J. Brangsch, A. Mohtashamdolatshahi, O. Kosch, H. Paysen, F. Wiekhorst, R. Klopffleisch, R. Buchholz, U. Karst, M. Taupitz, J. Schnorr, B. Hamm, and M. R. Makowski, Ex vivo magnetic particle imaging of vascular inflammation in abdominal aortic aneurysm in a murine model, *Sci. Rep.* **10**, 12410 (2020).
- [68] E. Y. Yu, M. Bishop, B. Zheng, R. M. Ferguson, A. P. Khandhar, S. J. Kemp, K. M. Krishnan, P. W. Goodwill, and S. M. Conolly, Magnetic particle imaging: A novel in vivo imaging platform for cancer detection, *Nano Lett.* **17**, 1648 (2017).
- [69] Z. W. Tay, P. Chandrasekharan, A. Chiu-Lam, D. W. Hensley, R. Dhavalikar, X. Y. Zhou, E. Y. Yu, P. W. Goodwill, B. Zheng, C. Rinaldi, and S. M. Conolly, Magnetic particle imaging-guided heating in vivo using gradient fields for arbitrary localization of magnetic hyperthermia therapy, *ACS Nano* **12**, 3699 (2018).
- [70] Q. Wang, X. Ma, H. Liao, Z. Liang, F. Li, Jie Tian, and D. Ling, Artificially engineered cubic iron oxide nanoparticle as a high-performance magnetic particle imaging tracer for stem cell tracking, *ACS Nano* **14**, 2053 (2020).
- [71] Z. G. Forbes, B. B. Yellen, D. S. Halverson, G. Fridman, K. A. Barbee, and G. Friedman, Validation of high gradient magnetic field based drug delivery to magnetizable implants under flow, *IEEE. Trans. Biomed. Eng.* **55**, 643 (2008).
- [72] D. Li and Y. Ren, High-gradient magnetic field for magnetic nanoparticles drug delivery system, *IEEE Trans. Appl. Supercond.* **28**, 4402107 (2018).
- [73] M. Graeser, F. Thieben, P. Szwargulski, F. Werner, N. Gdaniec, M. Boberg, F. Griese, M. Möddel, P. Ludewig, D. van de Ven, O. M. Weber, O. Woywode, B. Gleich, and T. Knopp, Human-sized magnetic particle imaging for brain applications, *Nat. Commun.* **10**, 1936 (2019).